Spatially and temporally resolved temperature and shock-speed measurements behind a laser-induced blast wave of energetic nanoparticles

Sukesh Roy, Naibo Jiang, Hans U. Stauffer, Jacob B. Schmidt, Waruna D. Kulatilaka, Terrence R. Meyer, Christopher E. Bunker, and James R. Gord

Articles you may be interested in

Nanoparticle generation and transport resulting from femtosecond laser ablation of ultrathin metal films: Time-resolved measurements and molecular dynamics simulations
Appl. Phys. Lett. **104**, 193106 (2014); 10.1063/1.4876601

Double shock front formation in cylindrical radiative blast waves produced by laser irradiation of krypton gas
Phys. Plasmas **20**, 123101 (2013); 10.1063/1.4838235

Blast wave and contraction in Au(111) thin film induced by femtosecond laser pulses. A time resolved x-ray diffraction study.
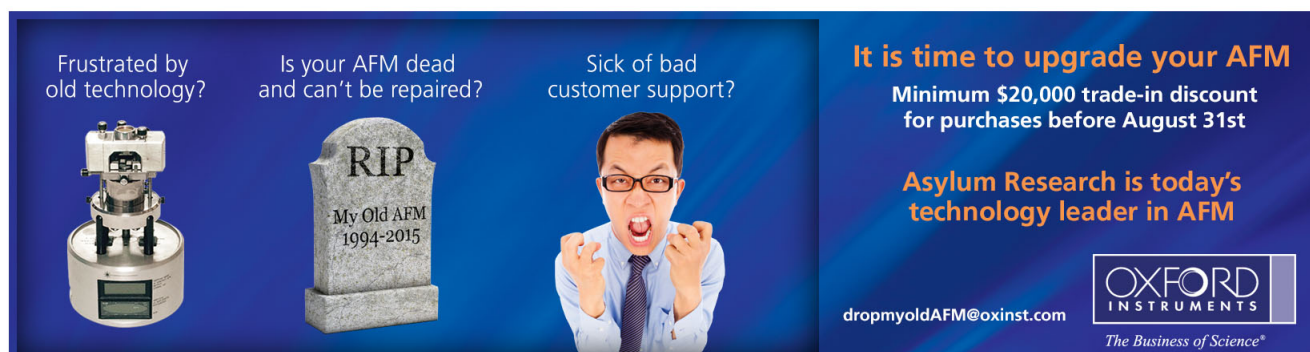J. Appl. Phys. **109**, 113522 (2011); 10.1063/1.3594732

Femtosecond coherent anti-Stokes Raman scattering measurement of gas temperatures from frequency-spread dephasing of the Raman coherence
Appl. Phys. Lett. **89**, 251112 (2006); 10.1063/1.2410237

Planar Laser-Induced Iodine Fluorescence Measurements in Rarefied Hypersonic Flow
AIP Conf. Proc. **762**, 1325 (2005); 10.1063/1.1941716

Spatially and temporally resolved temperature and shock-speed measurements behind a laser-induced blast wave of energetic nanoparticles

Sukesh Roy,[1,a] Naibo Jiang,[1] Hans U. Stauffer,[1] Jacob B. Schmidt,[1] Waruna D. Kulatilaka,[1] Terrence R. Meyer,[2] Christopher E. Bunker,[3] and James R. Gord[3]

[1]*Spectral Energies, LLC, 5100 Springfield Street, Dayton, Ohio 45431, USA*
[2]*Department of Mechanical Engineering, Iowa State University, Ames, Iowa 50011, USA*
[3]*Air Force Research Laboratory, Aerospace Systems Directorate, Wright-Patterson Air Force Base, Ohio 45433, USA*

Spatially and temporally resolved temperature measurements behind an expanding blast wave are made using picosecond (ps) N_2 coherent anti-Stokes Raman scattering (CARS) following laser flash heating of mixtures containing aluminum nanoparticles embedded in ammonium-nitrate oxidant. Production-front ps-CARS temperatures as high as 3600 ± 180 K—obtained for 50-nm-diameter commercially produced aluminum-nanoparticle samples—are observed. Time-resolved shadowgraph images of the evolving blast waves are also obtained to determine the shock-wave position and corresponding velocity. These results are compared with near-field blast-wave theory to extract relative rates of energy release for various particle diameters and passivating-layer compositions. © 2013 AIP Publishing LLC. [http://dx.doi.org/10.1063/1.4804410]

I. INTRODUCTION

Energetic nanomaterials represent the next frontier in the development of controllable energy release for use in explosives and propellants.[1] In particular, aluminum and boron exhibit considerable promise as high-energy-density species in the presence of oxidizers,[2] and the increasingly economical availability of aluminum nanoparticles, along with a variety of readily tunable physical properties, such as particle diameter and composition of passivation layer, make aluminum nanoparticles particularly attractive for further study.[1,3–7] When used as an additive in solid-rocket propellants or high explosives, aluminum particles are rapidly ejected into the gas phase following the initial impulsive combustion event; these particles then continue to react with oxidants present in that gas-phase mixture produced by the initial impulsive event.[8] The dynamics of aluminum-particle reactions in such gas-phase environments have been studied in depth by several groups, and a notable dependence of these reaction dynamics on particle size has been observed. In particular, for large aluminum particles (>10–$20 \, \mu$m), it has been observed that reaction rates are limited by timescales of oxidizer diffusion to the reaction front, whereas for nanometer-size particles these reactions are governed by kinetics of aluminum nanoparticles.[9–11] The use of nanoaluminum has also been shown to increase detonation velocities in some cases.[7]

Emission spectroscopy from the gas-phase reaction intermediate aluminum oxide (AlO) has been used to gauge reaction temperatures during gas-phase combustion of aluminum particles;[8,9] however, significantly less AlO is observed during the combustion of sub-micron-diameter particles,[12,13]

compromising its usefulness for making accurate temperature measurements. Furthermore, because AlO is expected to be present only in the highest temperature regions that contain reacting species, this approach provides only the peak temperature attained during the combustion process.[8] In the absence of significant AlO emission, an alternative multi-wavelength pyrometric approach that relies upon the Planckian gray-body emission from incandescent reacting particles has been used to estimate the temperature conditions associated with reacting aluminum-nanoparticle samples.[14] Both of these approaches yield an estimated uncertainty of ~150 K under peak temperature conditions and provide no spatial resolution and only limited temporal resolution of the reaction environment. Additionally, absorptive approaches have been used for continuous time-dependent measurement of temperature behind shock waves;[15] however, such measurements have not, to date, been applied toward the gas-phase oxidation of nanoaluminum and its oxidation products following laser flash heating.

We have applied picosecond coherent anti-Stokes Raman scattering (ps-CARS), which is a well-established non-invasive approach to measuring temperature in a reacting environment with excellent accuracy and precision,[16–19] to allow thermometric measurements of the gas-phase species in thermal equilibrium with reacting, energetic nanoparticle samples following laser flash heating. This point-wise detection approach permits spatially resolved measurements under single-laser-shot conditions, and the temporal resolution of this approach is limited only by the greater of the durations of the flash-heating laser [several nanoseconds (ns) in this work] and the sub-ns pulse durations used in the ps-CARS techniques. Furthermore, employing ps-duration lasers allows the concurrent use of time-resolved shadowgraphy to visualize the associated shock wave (or "blast wave") observed upon laser flash heating of these nanoparticle samples[20] and the

[a]Author to whom correspondence should be addressed. Electronic mail: sroy@woh.rr.com

associated time-dependent initial energy-release rates of several aluminum-nanoparticle samples embedded in ammonium-nitrate oxidant as a function of nanoparticle size (diameters ranging from 18 to 80 nm). Thus, these measurements represent a significant advancement in resolving, both spatially and temporally, the energy-release rates and temperatures encountered by energetic nanomaterials during oxidation in a gas-phase environment.

II. EXPERIMENTAL

Three sizes of Al_2O_3-passivated aluminum nanoparticles were used during the course of these experiments, including nominal particle diameters of 18 nm (Skyspring Nanomaterials, Inc.), 50 nm (MTI Corporation), and 80 nm (synthesized at Edwards Air Force Base). Additionally, oleic-acid-passivated core-shell aluminum nanoparticles (30-nm diameter), produced via sonochemical methods,[21–24] were also studied for comparison purposes; these will be referred to below as 30-nm AlOA. Transmission-electron-microscopy (TEM) images of these samples show a broad size distribution of spherical nanoparticles, with average sizes close to the corresponding nominal diameters. In all experiments described here, solid sample pellets were created using 20%:80% mixtures (by weight) of aluminum-nanoparticle fuel in ammonium-nitrate (Sigma Aldrich) oxidizer. Each 5-mm-diameter, circular sample pellet contained ∼10 mg of fuel-oxidizer mixture; their preparation is described elsewhere.[24]

The experimental configuration used for the ps-CARS thermometric measurements is depicted schematically in Fig. 1, and the ps-CARS optical setup has been described in detail previously.[17] Briefly, it consists of a ps-duration, pulsed Nd:YAG laser (Ekspla, Model SL230) that operates at 10 Hz and produces nearly transform-limited pulses [full-width-at-half-maximum (FWHM) duration of ∼150 ps and

maximum pulse energy of 100 mJ/pulse] at 532 nm; this beam is split into pump and probe beams, each with an energy of 800 μJ/pulse. A fraction of this laser output is also split off to pump a home-made modeless dye laser (FWHM bandwidth of ∼5 nm and FWHM duration of ∼110 ps) for generating the Stokes beam at 606 nm with an energy of 3 mJ/pulse. The pump, probe, and Stokes beams are arranged in a folded-BOXCARS geometry, and the temporal overlap is adjusted using translation stages in the paths of the pump and probe beams. The Rayleigh length of the overlapped ps-CARS beams is estimated to be ∼0.5 mm. The spatial resolution of this optical setup in the z-direction (normal to the sample surface) is estimated to be 30 μm. The CARS signal beam is directed into a 1.25-m spectrometer (SPEX 1250M) that is equipped with a 2400-groove/mm grating, and the resultant dispersed spectrum is recorded using a back-illuminated 2048 × 512-pixel-array CCD camera with full vertical binning (Andor Technologies Model DU 440BU). The measured spectral resolution of the CARS detection system is ∼0.54 cm^{-1}, which is similar to the typical spectral resolution for ns-CARS systems and is sufficient to resolve the rovibrational transitions under the current reaction conditions. Laser flash heating of the samples was achieved using the ns-duration 532-nm output from a separate Nd:YAG laser (10-ns pulse duration) reduced to a 1.5-mm-diameter spot at the surface of the sample pellet with an estimated fluence of 0.3 J/cm^2. By controlling the delay time between the flash-heating beam and the three time-overlapped ps-CARS beams as well as the height of the nanoparticle pellet, we have the ability to obtain the spatiotemporally resolved temperatures of the nitrogen gas in equilibrium with the reacting, energetic nanoparticle samples. Additionally, time-resolved shadowgraph images following flash heating were obtained using the ps-duration dye-laser pulse as a light source and an intensified CCD camera with a 30-ns exposure gate for imaging. Each shadowgraph image corresponds to a single flash-heating event, with a fixed time delay between the flash-heating laser and the shadowgraph-light-source laser; the sample pellet was rotated between laser shots to provide a fresh sample surface for each shadowgraph image. The uncertainty in the position of the shock wave was found to be ∼±2%, resulting primarily from the observed width of the shock wave in the shadowgraph images. The reproducibility of the observed shock-wave positions was determined by making multiple single-shot measurements at several time delays; this reproducibility was found to fall within the ±2% uncertainty range.

III. RESULTS AND DISCUSSION

A. Temporally resolved shadowgraphy of shock propagation

Time-resolved shadowgraph images were recorded for each aluminum-nanoparticle sample to track the initial formation and subsequent evolution of the shock wave that follows the laser flash heating of these materials. A sample series of shadowgraph images is shown in Fig. 2 for 50-nm aluminum nanoparticles embedded in ammonium nitrate. A single strong shock boundary is not observed at the earliest

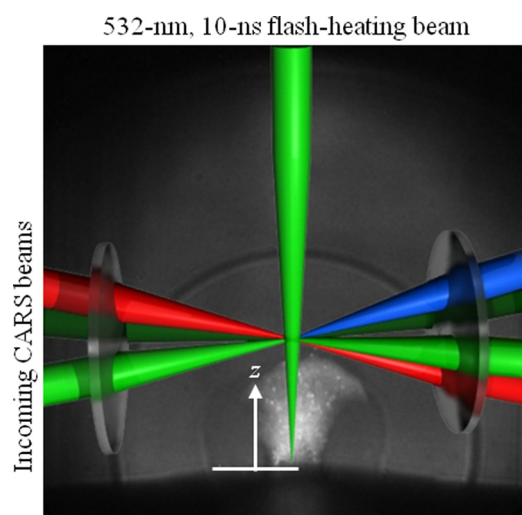532-nm, 10-ns flash-heating beam

Incoming CARS beams

FIG. 1. Composite picture depicting the optical configuration used in ps-CARS temperature measurements following laser flash heating of energetic nanomaterial samples. A ns-duration flash-heating laser impinges on the sample from above; three incoming ps-duration CARS beams overlap at a point above the sample surface (along the z-axis dimension), producing a fourth outgoing CARS signal beam. Pictorial overlays within the image include an example shadowgraph of a shock wave and an example reacting-plume Mie-scattering image to provide reference.
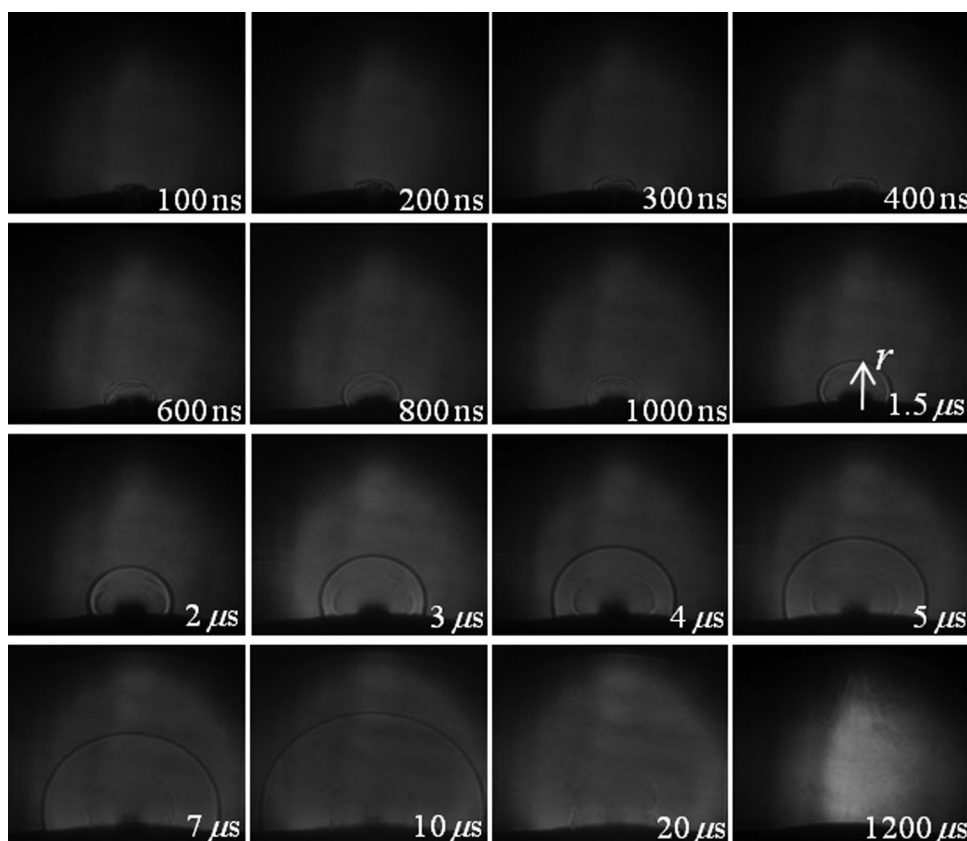
FIG. 2. Shock-wave evolution following laser flash heating of samples containing 50-nm aluminum nanoparticles embedded in ammonium nitrate. Full-frame image height is 105 mm.

time delays (<1000 ns); instead, a diffraction pattern containing light and dark stripes is observed before coalescing into a sharper leading shock boundary at longer delays. It should be noted that similar features have been observed in the early stages of material ejection during laser ablation of aluminum using intense (∼40 J/cm^2) femtosecond laser pulses; in that case, the diffraction is attributed to the cooling process associated with initially ejected ablated material following rapid overheating (estimated temperature ∼10^5 K) of the material surface.[20] In contrast, the initial flash-heating process under low-laser-fluence (∼0.3 J/cm^2) conditions used here is expected to produce significantly less initial heating of the absorbing aluminum nanoparticle, with temperatures ranging between the melting point (933 K) and the boiling point (2740 K) of aluminum.[3,25] The presumed mechanism for reaction of these heated aluminum nanoparticles then follows a sequence involving the breakdown of the surrounding passivation layer, the initiation of a reaction sequence between the heated aluminum and the surrounding solid-oxidant substrate material, and subsequent sustained solid-phase exothermic reactions that produce heat and light and eject aluminum nanoparticles into the surrounding environment to react with oxidants present in the gas-phase mixture.[3] At longer time delays, this explosive ejection of material from the sample surface is observed—as was the case for all experimental samples studied here—as an expanding dark plume emanating from the sample surface. Mie-scattering measurements, as depicted in Fig. 1, provide much clearer images of this evidence of reactive oxidation following laser flash heating of the nanoparticles.

The corresponding time-dependent shock-wave position was observed to change for the different nanoparticle samples,

as shown in Fig. 3(a), with the 50-nm commercial aluminum-nanoparticle samples exhibiting the most rapid shock-wave expansion over the first 10 μs. Prior studies concerned with probing the shock-wave velocities associated with a variety of laser-initiated expansions, including ablation and plasma-forming processes,[20,26–28] have used classical Taylor-Sedov (T-S) blast-wave theory[29–31] or modified variations thereof that account for drag forces associated with the surrounding medium.[26,27] Classical T-S theory assumes that an initial instantaneous input of energy produces a shock wave that is emitted from a point source, which results in a simple expression for the time (t) dependence of the expanding shock-front radius, r, as follows:

$$r = C(E_0/\rho_0)^{1/5}t^{2/5}, \qquad (1)$$

where E_0 is the initial constant-energy input, ρ_0 is the density of the ambient surrounding gas, and C is a constant related to the specific-heat ratio, γ, of the gas swept up by the shock wave.[32] A more generalized, time-dependent energy-release-rate model has also been developed to describe variable-energy blast waves, assuming a time-dependent energy, E, of the form

$$E(t) = At^\beta, \qquad (2)$$

where A and β are condition-dependent constants;[33,34] and $\beta = 0$ corresponds to the classical T-S blast-wave-theory limit. Moreover, classical T-S blast-wave theory is only strictly valid within a regime in which the mass of the energy source is negligible compared to the mass of the ambient surrounding gas that is swept up by the expanding shock. This
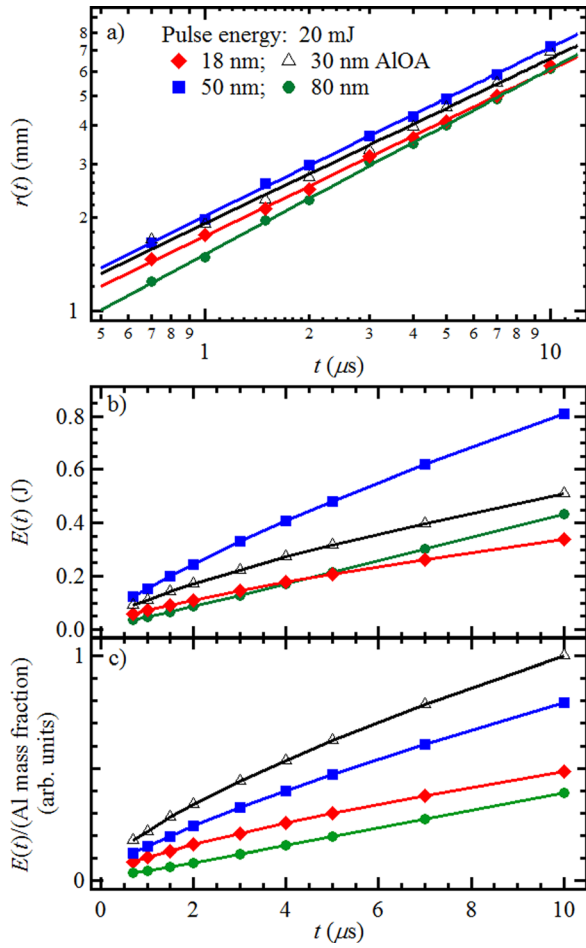
FIG. 3. (a) Time-dependent shock-wave position, *r*, depicted as symbols for four aluminum nanoparticle samples; curves correspond to power-law least-squares fits. (b) Corresponding calculated time-dependent energy release for the four denoted aluminum nanoparticle samples. (c) Comparison of energy released, normalized for mass fraction of aluminum in each sample. In (b) and (c), symbols are connected by line segments for clarity.

assumption is inherently invalid during the very earliest stages of shock expansion, and near-field variants of this theory have been developed to account for the mass contribution of the point source.[32,35,36] In particular, for spherical shock waves expanding in three dimensions, a near-field description of the relationship between the source energy and the expanding shock radius takes the form

$$E = (K_1 + K_2 r^3)\left(\frac{dr}{dt}\right)^2, \tag{3}$$

where the constants K_1 and K_2 contain source debris and surrounding gas-phase-medium parameters as follows:[32]

$$K_1 = \frac{8\pi\rho_s R_s^3}{3(\gamma+1)^2}, \tag{4a}$$

$$K_2 = \frac{8\pi\rho_0(3\gamma-1)}{3(\gamma+1)^2(\gamma-1)}. \tag{4b}$$

In these expressions, ρ_s denotes the density of the solid source material, and R_s denotes the initial source radius of an

assumed sphere of material that is producing the shock wave. In this expression, it is assumed that the heat-capacity ratio, γ, associated with the source debris is equal to the surrounding heat-capacity ratio. It should be noted that in the limit where the source mass becomes negligible compared to the mass of air swept up by the expanding shock wave, $K_1 \ll K_2 r^3$, and Eq. (3) reduces to an expression that is consistent with the constant-energy-source classical T-S theory expression shown in Eq. (1), albeit with an additional contribution to the total initial energy from energy contained within the source debris.[32,36]

For all samples studied here, the observed expanding shock wave radius was found to exhibit an approximate power-law dependence on time, as demonstrated by the observed linearity in the log–log plots depicted in Fig. 3(a). Therefore, each data set was fit to a power-law dependence of the form

$$r(t) = At^\alpha. \tag{5}$$

The extracted *A* and α fitting parameters were then employed to calculate the time-dependent energy using Eq. (3), with $\rho_0 = 1.20\,\text{kg/m}^3$ and $\gamma = 1.4$ for room-temperature air; the values used for the solid-phase components were estimated to be $\rho_s = 1750\,\text{kg/m}^3$ and $R_s = 1.0 \times 10^{-4}\,\text{m}$, and it was assumed that the combustion-reaction heat-capacity ratio was comparable to that of room-temperature air (i.e., $\gamma = 1.4$). Under these conditions, $K_1 \ll K_2 r^3$ over the observed timescales and corresponding shock-wave radii, and the calculated released energy over the observed timescale takes the approximate form

$$E(t) = K_2 A^5 \alpha^2 t^{(5\alpha-2)}, \tag{6}$$

which is consistent with the variable-energy blast-wave model assumption shown in Eq. (2). The corresponding calculated time-dependent energies released by the four studied nanoparticle samples following flash heating are shown in Fig. 3(b). We note that although the estimated nature of these solid-phase and debris-field quantities results in uncertainty in the absolute magnitudes of these energy-release values—particularly under the assumption that the source-debris and ambient-gas heat capacities are equivalent—such estimates allow comparison of the relative magnitudes of these quantities from sample to sample. In particular, it was observed that the oxide-passivated 50-nm samples exhibited the most rapid energy release over the observed timescales, whereas the 18-nm and 80-nm samples exhibited notably less released energy. It is also important to note that the presence of passivating surface species (alumina in the case of the 18-nm, 50-nm, and 80-nm samples and a combination of alumina and an organic surface-bound species in the case of the 30-nm AlOA samples) results in varying aluminum compositions among the tested samples. To account for the relative compositions of aluminum available for oxidative reaction in these samples, we assume that the spherical alumina-passivated species have a uniform 2.5-nm alumina outer shell; measurements showed the 30-nm AlOA samples to contain ~40% Al.[21] As depicted in Fig. 3(c), when the relative mass fractions of aluminum are taken into account, the
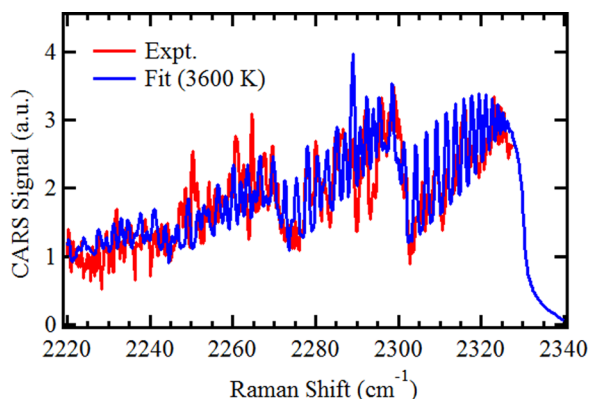
FIG. 4. Example single-shot N_2 ps-CARS spectrum following flash heating of sample containing 50-nm aluminum nanoparticles. The included theoretical spectrum was calculated using the modified Sandia CARSFT code with an assumed temperature of 3600 K.

30-nm AlOA samples exhibit the highest energy release per aluminum mass fraction among the tested samples.

B. Temporally and spatially resolved temperature behind shock waves

A typical single-laser-shot nitrogen ps-CARS spectrum is shown in Fig. 4; this spectrum was acquired for the 50-nm-particle sample at $z = 0.5$ mm above the sample surface and a delay of 350 nm after flash heating. For this and all ps-CARS measurements, the temperature was evaluated by least-squares fitting of the experimental spectrum with a theoretical spectrum that was calculated using the Sandia CARSFT code;[37] here, a best-fit temperature of 3600 $\pm$ 180 K is observed. As noted above, the ability to make point-wise measurements using ps-CARS affords, for the first time in a reacting energetic-materials sample, the ability to map the spatial temperature distribution as a function of time. Figure 5 displays an example of such spatially resolved temperatures measured behind a blast wave that is induced by the laser flash heating of samples containing 50-nm aluminum nanoparticles. Overlaid within this figure is an example shadowgraph image that was obtained 1.3 μs after flash

heating of the sample; the resultant blast-wave radius is $\sim$2.3 mm at this delay. Single-shot CARS temperature measurements were made at $z = 1.25$ mm, 1.5 mm, and 1.75 mm above the surface of the sample pellet at this delay, and the measured temperatures were found to be 3000 K, 1450 K, and 1150 K, respectively, with corresponding uncertainties of $\pm$5%.

To address the spatially resolved temperatures observed behind the shock wave, we invoke a simple model based on the measured shock velocity. Hendijanifard and Willis have derived straightforward expressions for the temperatures and pressures expected *directly* behind a low-Mach-number shock wave based on measured shock-wave speeds by solving the standing normal shock equations of momentum, continuity, energy, and state.[38] Based on those expressions and the measured shock-wave velocity determined for this sample by differentiation of Eq. (5), we calculate the temperature directly behind the shock wave under these conditions to be 766 K. Unfortunately, it is challenging to use the ps-CARS approach for measuring temperature immediately behind the shock front because of the significant changes in the gas-phase refractive index associated with large density changes; therefore, a direct comparison between this theoretical value and experiment cannot be made. However, under the simplifying assumption that the shock-induced temperature at a given position remains essentially constant following passage of the shock-wave front, it is possible to estimate the position-sensitive temperature based on the calculated temperature directly behind the shock front at the moment the shock passed a given position. This calculated temperature dependence is depicted in Fig. 6, assuming the fitted shock-wave-position time dependence [Eq. (5)] for the 50-nm aluminum nanoparticle sample; this theoretical curve corresponds to the calculated temperature behind the shock wave plotted as a function of shock-wave position. At positions nearer the shock front, this simple theoretical model agrees reasonably well with the measured temperatures, whereas the experimentally observed temperatures show positive deviation from this theoretical value at greater distances behind the shock wave. Such deviation may be indicative of the cumulative effects of additional time-dependent heat
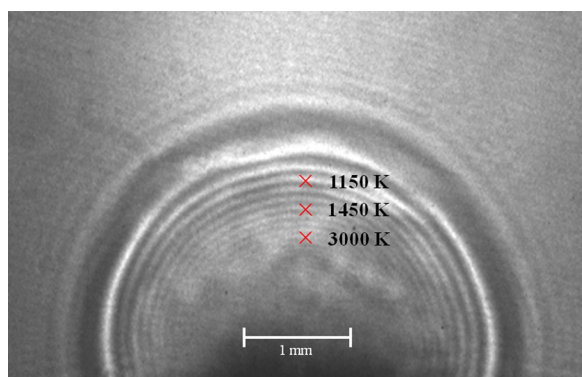

FIG. 5. Spatially resolved ps-CARS temperatures measured for 50-nm nanoparticle samples shown with respect to a measured shadowgraph image. All depicted measurements were made at a delay of 1.3 μs after flash heating. At this delay, the shock-wave radius is 2.33 mm, and the three temperature measurements correspond to heights of $z = 1.25$, 1.5, and 1.75 above the sample surface.
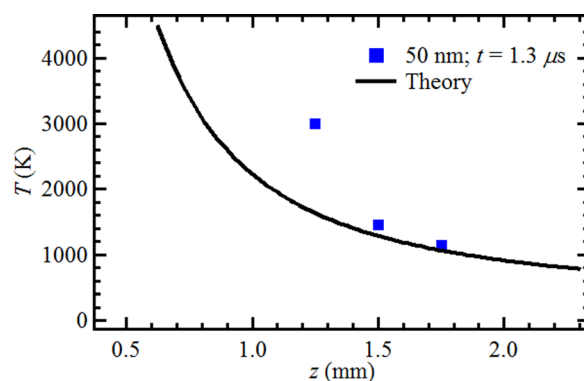

FIG. 6. Comparison of observed ps-CARS (symbols) and theoretical (curve) temperatures for samples containing 50-nm nanoparticles at several distances, z, above the sample at a delay of 1.3 μs after flash heating. Theoretical temperature is determined based on the measured shock-wave position as a function of time.
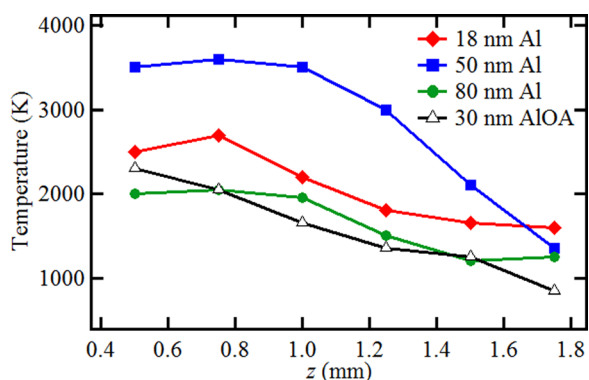
FIG. 7. Temperature at reaction-plume front observed for four aluminum-nanoparticle samples.

release as the sample-oxidation process evolves, resulting in an additional temperature increase in the ambient gas as time progresses.

Additionally, we note that a darker area is observed within the shadowgraph image shown in Fig. 5, indicating the presence of a reaction plume that contains the solid debris ejected from the sample after the initial explosive reaction occurs. Mie-scattering images associated with this same sample material under these conditions demonstrate that the reaction plume reaches a distance of $z = 1.2$–1.3 mm at a delay of $1.3\ \mu$s. Unfortunately, we found that the optical density of this ejected material was sufficient to prevent ps-CARS measurements at distances inside this leading edge, and we were unable to measure temperature directly within the expanding debris field.

Finally, to gauge the temperatures encountered by the ejected nanoparticle samples as they move into the gas phase following the initial explosive reaction, we used ps-CARS to measure the temperatures directly in front of the reaction plume at several time delays for the four samples. The resultant temperatures are shown in Fig. 7 as a function of the leading edge of the reaction plume. Consistent with the time-dependent energy release determined from the shock-wave velocities, the 50-nm nanoparticle samples were observed to experience the greatest temperature increases in the surrounding gas-phase environment, and the resulting expanding reaction plume encountered the highest gas-phase temperatures. All samples were observed to encounter temperatures exceeding the aluminum melting point (933 K), and the 50-nm particle samples encountered temperatures exceeding both the alumina (Al_2O_3) melting point ($\sim$2300 K)[12] and the boiling point of aluminum (2740 K). Under such conditions, it is expected that the nanoparticles continue to undergo rapid reaction with gas-phase oxidant species that are present in this environment, including ambient oxygen as well as the decomposition products of the initial solid-phase oxidation reactions between aluminum and ammonium nitrate.

IV. CONCLUSIONS

Nitrogen ps-CARS has been used to provide, for the first time, simultaneous temporally and spatially resolved temperature measurements behind an expanding blast wave. These measurements, made at several times and positions following

the flash heating of energetic aluminum nanoparticles embedded in ammonium nitrate, allow determination of the range of temperatures encountered by particles following ejection into the surrounding gas-phase medium. Temperatures as high as 3600 K were observed at the reaction-plume front when 50-nm-diameter commercial aluminum-nanoparticle samples were used. These temperatures, measured at positions near the expanding shock-wave-front position that was determined using time-resolved shadowgraphy, were shown to be consistent with position-dependent temperatures calculated using exact low-Mach-number temperature and pressure relationships across a shock wave with a known time-dependent speed. In contrast, these simple calculations underestimate the temperatures observed at positions further behind the shock wave, most likely because of additional heat produced during the continued reactivity of the energetic nanoparticle samples.

[1]E. L. Dreizin, Prog. Energy Combust. Sci. **35**, 141 (2009).
[2]D. D. Dlott, Mater. Sci. Technol. **22**, 463 (2006).
[3]Y. Yang, Z. Sun, S. Wang, and D. D. Dlott, J. Phys. Chem. B **107**, 4485 (2003).
[4]K. Park, D. Lee, A. Rai, D. Mukherjee, and M. R. Zachariah, J. Phys. Chem. B **109**, 7290 (2005).
[5]A. N. Ali, S. F. Son, B. W. Asay, and R. K. Sander, J. Appl. Phys. **97**, 063505 (2005).
[6]V. E. Sanders, B. W. Asay, T. J. Foley, B. C. Tappan, A. N. Pacheco, and S. F. Son, J. Propul. Power **23**, 707 (2007).
[7]P. Brousseau and C. J. Anderson, Propellants, Explos., Pyrotech. **27**, 300 (2002).
[8]N. Glumac, H. Krier, T. Bazyn, and R. Eyer, Combust. Sci. Technol. **177**, 485 (2005).
[9]T. Bazyn, H. Krier, and N. Glumac, Proc. Combust. Inst. **31**, 2021 (2007).
[10]A. A. Abdel-Hafez, M. W. Brodt, J. R. Carney, and J. M. Lightstone, Rev. Sci. Instrum. **82**, 064101 (2011).
[11]R. A. Yetter, G. A. Risha, and S. F. Son, Proc. Combust. Inst. **32**, 1819 (2009).
[12]T. Bazyn, H. Krier, and N. Glumac, Combust. Flame **145**, 703 (2006).
[13]P. Lynch, G. Fiore, H. Krier, and N. Glumac, Combust. Sci. Technol. **182**, 842 (2010).
[14]D. S. Moore, S. F. Son, and B. W. Asay, Propellants, Explos., Pyrotech. **29**, 106 (2004).
[15]M. A. Oehlschlaeger, D. F. Davidson, and J. B. Jeffries, Appl. Opt. **44**, 6599 (2005).
[16]S. Roy, T. R. Meyer, and J. R. Gord, Opt. Lett. **30**, 3222 (2005).
[17]S. Roy, T. R. Meyer, and J. R. Gord, Appl. Phys. Lett. **87**, 264103 (2005).
[18]T. R. Meyer, S. Roy, and J. R. Gord, Appl. Spectrosc. **61**, 1135 (2007).
[19]S. Roy, J. R. Gord, and A. K. Patnaik, Prog. Energy Combust. Sci. **36**, 280 (2010).
[20]N. Zhang, X. N. Zhu, J. J. Yang, X. L. Wang, and M. W. Wang, Phys. Rev. Lett. **99**, 167602 (2007).
[21]K. A. S. Fernando, M. J. Smith, B. A. Harruff, W. K. Lewis, E. A. Guliants, and C. E. Bunker, J. Phys. Chem. C **113**, 500 (2009).
[22]C. E. Bunker, M. J. Smith, K. A. S. Fernando, B. A. Harruff, W. K. Lewis, J. R. Gord, E. A. Guliants, and D. K. Phelps, ACS Appl. Mater. Interfaces **2**, 11 (2010).

[23]W. K. Lewis, A. T. Rosenberger, J. R. Gord, C. A. Crouse, B. A. Harruff, K. A. S. Fernando, M. J. Smith, D. K. Phelps, J. E. Spowart, E. A. Guliants, and C. E. Bunker, J. Phys. Chem. C **114**, 6377 (2010).

[24]W. K. Lewis, B. A. Harruff, J. R. Gord, A. T. Rosenberger, T. M. Sexton, E. A. Guliants, and C. E. Bunker, J. Phys. Chem. C **115**, 70 (2011).

[25]Y. Yang, S. Wang, Z. Sun, and D. D. Dlott, J. Appl. Phys. **95**, 3667 (2004).

[26]T. A. Schmitz, J. Koch, D. Gunther, and R. Zenobi, J. Appl. Phys. **109**, 123106 (2011).

[27]X. Chen, B. M. Bian, Z. H. Shen, J. Lu, and X. W. Ni, Microwave Opt. Technol. Lett. **38**, 75 (2003).

[28]X. Z. Zeng, X. L. Mao, S. S. Mao, S. B. Wen, R. Greif, and R. E. Russo, Appl. Phys. Lett. **88**, 061502 (2006).

[29]G. I. Taylor, Proc. R. Soc. London, Ser. A **201**, 159 (1950).

[30]Y. B. Zel'dovich and Y. P. Razier, *Physics of Shock Waves and High-Temperature Hydrodynamic Phenomena* (Academic Press, New York, 1966).

[31]C. E. Needham, *Blast Waves* (Springer, 2010).

[32]D. A. Freiwald and R. A. Axford, J. Appl. Phys. **46**, 1171 (1975).

[33]R. A. Freeman, J. Phys. D: Appl. Phys. **1**, 1697 (1968).

[34]H. Steiner, W. Gretler, and T. Hirschler, Shock Waves **8**, 139 (1998).

[35]G. J. Hutchens, J. Appl. Phys. **77**, 2912 (1995).

[36]G. J. Hutchens, J. Appl. Phys. **88**, 3654 (2000).

[37]R. E. Palmer, "The CARSFT computer code for calculating coherent anti-stokes Raman spectra: User and programmer information," Report No. SAND89-8206 (1989).

[38]M. Hendijanifard and D. A. Willis, J. Phys. D: Appl. Phys. **44**, 145501 (2011).